applied sciences

MDPI

Article

Scan-Less Line Field Optical Coherence Tomography, with Automatic Image Segmentation, as a Measurement Tool for Automotive Coatings

Samuel Lawman [1,2], Bryan M. Williams [2], Jinke Zhang [1], Yao-Chun Shen [1,*] and Yalin Zheng [2]

[1] Department of Electrical Engineering and Electronics, University of Liverpool, Liverpool L69 3GJ, UK; S.Lawman@liverpool.ac.uk (S.L.); sgjzhan5@student.liverpool.ac.uk (J.Z.)
[2] Department of Eye and Vision Science, University of Liverpool, Liverpool L7 8TX, UK; Bryan.Williams@liverpool.ac.uk (B.M.W.); Yalin.Zheng@liverpool.ac.uk (Y.Z.)
* Correspondence: Y.C.Shen@liverpool.ac.uk; Tel.: +44-(0)151-794-4575

Academic Editor: Michael Pircher
Received: 3 February 2017; Accepted: 29 March 2017; Published: 1 April 2017

Abstract: The measurement of the thicknesses of layers is important for the quality assurance of industrial coating systems. Current measurement techniques only provide a limited amount of information. Here, we show that spectral domain Line Field (LF) Optical Coherence Tomography (OCT) is able to return to the user a cross sectional B-Scan image in a single shot with no mechanical moving parts. To reliably extract layer thicknesses from such images of automotive paint systems, we present an automatic graph search image segmentation algorithm. To show that the algorithm works independently of the OCT device, the measurements are repeated with a separate time domain Full Field (FF) OCT system. This gives matching mean thickness values within the standard deviations of the measured thicknesses across each B-Scan image. The combination of an LF-OCT with graph search segmentation is potentially a powerful technique for the quality assurance of non-opaque industrial coating layers.

Keywords: optical coherence tomography; coatings; spectral domain; time domain; quality assurance; line field; image segmentation; graph search

1. Introduction

Non-opaque coatings are used to provide protection and aesthetic enhancement to a wide variety of objects in many contexts. Examples of this variety are the heavy industry clear top coats in modern car paint systems [1], the do-it-yourself varnishing of outdoor wooden objects [2], and the highly specialised varnish coatings for valuable works of art [3]. This paper is focused on the economically important industrial coating context [1,4]. The term Quality Assurance (QA) [5] refers to the broad systems that ensure consistent quality of any (tangible or intangible) produced product. The appropriate processes and measures required are dependent on what that product is. To ensure that the layers of industrial coatings, such as automotive paint systems, give the desired protection and appearance, QA inspection methods that are capable of quantifying, and thus checking, the applied coating thickness and uniformity are required. However, it would be impractical to measure the thickness of the coating layers over the whole car body surface of every car produced on an automobile production line. Instead, to catch errors in the production process, sample measurements of thicknesses and consistency at appropriate points (spatial and temporal) are sufficient. To meet this need, a variety of instruments have been developed and are now available commercially. These commercially available instruments fall into two main categories. Magnetic and eddy current systems give a contact, single point measurement of coatings on metallic substrates [6]. They cannot be used with non-metallic

substrates and cannot give the thicknesses of multiple layers nor the uniformity of the coatings. The other category of commercially available systems are Ultrasound probe systems [6], which are able to measure independently of coatings on various substrates and can measure multiple layers. Though used widely for imaging in medicine [7], the ultrasound probe systems currently commercially available for coating measurements remain limited to a single point A-Scan. Manual scanning of probe can be performed by the user during repeat measurements. Remote ultrasound, such as laser ultrasonic methods [8], has been an area of research for coating measurements [9]. However, the added complexity of the device would add significantly to the cost and reduce portability.

Terahertz (THz) imaging has the ability to image the majority of coatings [10] but would be a relatively expensive solution due to the specialised band of electromagnetic (EM) radiation used. Optical confocal microscopy [11] instruments are able to characterise coatings, but remain expensive. Reflectometry [12] and ellipsometry [13] are prevalent in high tech thin film applications for measuring the thicknesses of multiple clear layers from interference effects. However, they are not prevalent for the measurement of industrial coatings.

Amongst Optical Coherence Tomography (OCT) applications outside of bio-medicine [14] is the non-contact measurement of the layers of paintings [15] and wooden artefacts [16], both commonly including optically transparent (varnish) layers. It has also been used to for the QA of transparent layer composited gradient refractive index optical components [17]. Following its use for measuring coating layers in the art conservation field, OCT has recently been considered for its potential QA applications [18] and for forensic use [19] for measuring the coating layers of automotive paints (an industrial field). Like THz imaging, the cost of general laboratory OCT systems is relative high (>£10,000). However, unlike THz imaging, OCT works at visible or near infrared wavelengths with a wide variety of low cost components available off the shelf. For the specific undemanding task of resolving thicknesses of transparent and semi-transparent coatings, much of an OCT device could be down-engineered to reduce cost.

Although a single A-Scan OCT device could be constructed to reduce cost, this would be undesirable for two reasons. Firstly, in this paper we will demonstrate a scenario in which a single A-Scan measurement gives erroneous results and only partial layer information. Multiple measurements of a sample may be required from the user for reliable results. Secondly, a B-Scan image gives more information than single A-Scans, such as a one-dimensional map of coating thickness and surface profile over the length of the measurement [20] and the ability to resolve additional scattering layers that would not be discernible from a single A-scan. However, the majority of OCT systems are optical fibre based measuring a single lateral point at a time. This conventional point by point raster scanning format requires a galvo mirror system(s). This adds to the mechanical complexity, including management of electrical and mechanical response issues [21], and cost of the system. Several alternative formats of OCT devices exist that measure more than one lateral position at a time without the need for mechanical scanning [22–24]. The form considered here is spectral domain Line Field (LF) OCT [25] which measures a B-Scan image in a single shot without moving parts. Though this format has been previously used for imaging in human [26,27] and animal [28,29] in vivo studies, and more recently for the QA of glass [30], the technique has not been previously applied in the measurement of industrial coatings.

Image segmentation [31–34] can break up images into their different regions, thus allowing their automated measurement. In practice, segmentation is often achieved by the thresholding of intensity values [35] at a parameter which may be selected either manually and empirically or automatically [36]. While this can yield results quickly and may be favoured particularly for large datasets, such parameters often require trial-and-error testing and vary between images. It is not well suited to problems involving poorly-defined boundaries, varying contrast, and visibility of noise, which are all characteristic of logarithmic OCT images in general. To address this limitation, many solutions have been proposed such as variational modelling [32,37–39] and machine learning approaches [33,40]. Recently, graph search algorithms have emerged as a popular [41–44] approach

for image segmentation due to the low computational energy required, reduced requirements for optimisation, and no need for training data.

Here we report the combined use of LF-OCT to acquire a cross sectional B-Scan image without electro-mechanical scanning, and a graph search sectioning algorithm to measure the clear coat and metallic base coat thickness for four automobile paints. The LF-OCT means that the image is taken in a single shot, with no scanning required. We show that graph search is a robust segmentation method for the measurement of layer thicknesses by OCT devices. The image quality and segmentation algorithm robustness was verified using images taken from the same car paint samples using a time domain Full Field (FF) OCT system. As an independent system based on the same physical principles as the LF-OCT system, the FF-OCT, which has previously been validated and calibrated using micro-X-CT [45], results served to show that no systematic experimental setup or calibration error was present in the system, and that any modality of OCT system will give similar results, with the graph search method applicable to them all. Correspondence with ultrasound and microscopy measurements has previously been shown for one type of OCT [18].

2. Materials and Methods

2.1. Optical Coherence Tomography Systems

The details of the LF-OCT used for this study has been previously described [46]. In brief, in order to measure an OCT B-Scan image in a single shot, a line was illuminated on the sample and reference surface, as shown in Figure 1 (left). This line was then imaged onto the slit of an imaging spectrograph, which resolved the interference spectrum at each position. A single (unaveraged) image was taken with the Back Illuminated Charged Couple Device (BI CCD) camera (iVac, Andor, Belfast, UK) and the Fourier phase differential mask method was used to supress aberration induced image artefacts. The band-pass filtered supercontinuum light source provided an axial resolution of 2.1 $n_G \cdot \mu m$, the plot of the point spread function is given in Figure 2 of [46]. With a 4f arrangement of 75 mm Achromatic pair (AC) objective (Linnik pair) and 100 mm AC collection lenses, the system's lateral resolution was measured to be 18 µm (United States Air Force 1951 resolution test chart (MIL-STD-150A), line pair width resolved).

To cross validate the OCT B-Scan images, a development of a previously presented [45] FF-OCT system was also used and is shown in Figure 1 (right). This time domain OCT system used an inexpensive infrared LED light source with a central wavelength of 850 nm and a bandwidth of 80 nm. The light was collimated for the illumination of the sample and reference mirror. The imaging optics was again a 4f arranged pair (objective F = 50 mm and collection F = 250 mm) of achromatic lenses, but with both situated behind the beam splitter. The panels were mounted on a high precision piezo motor positioner (LPS-65/N-565, Physik Instrumente, Bedford, UK) to scan in the axial direction. A high-speed USB 3.0 Complementary Metal Oxide Semiconductor (CMOS) camera (GS3-U3-23S6M-C, Point Grey, Richmond, British Columbia, Canada) was then used to collect the three-dimensional time domain interference data. During processing of the time domain FF-OCT data, the raw axial signal was convolved with a near ideal measured signal from a mirror. This increased the Signal to Noise Ratio (SNR), but at the cost of a slight detriment to axial resolution. The achieved lateral resolution of this system was significantly better (4.4 µm) than the LF-OCT system, though the axial resolution was worse (3.6 $n_G \cdot \mu m$).

Table 1 gives a summary of the performance of the two instruments. The time to take a measurement with the LF-OCT system was 60 ms, which is more than sufficient for a QA thickness measurement tool. The speed was limited by the mechanical shutter for the CCD camera, with the total illuminating light power physically attenuated accordingly. If required, the acquisition time could be shortened by orders of magnitude by using electronically shuttered CMOS cameras or using a single super-continuum pulse [46]. The 40 s acquisition time for the FF-OCT system would be too long for a practical QA tool. The FF-OCT provided a 3D volume measurement, however, for thickness

measurement we show here that the 2D B-Scan of the LF-OCT was sufficient to provide reliable layer thickness measurement values. The raw SNR and sensitivity values of the Fourier domain LF-OCT were higher than the time domain FF-OCT.

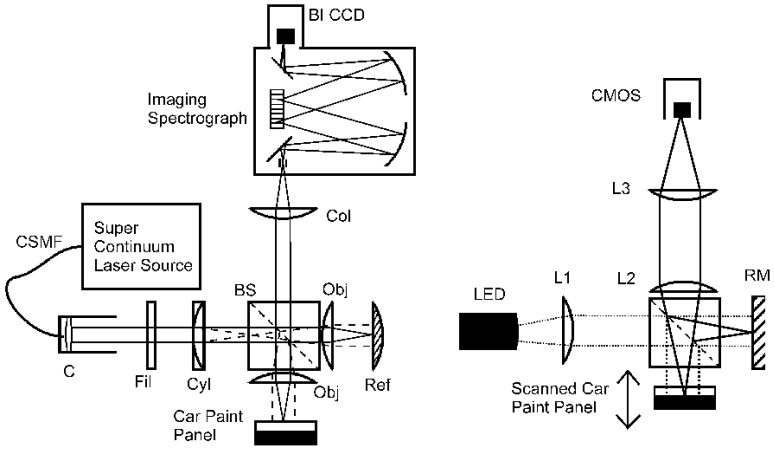

Figure 1. (**Left**) Line Field Optical Coherence Tomography (LF-OCT) setup. CSMF—Continuously Single Mode Fibre. C—Collimator, Fil—Optical Filters (Bandpass and Neutral Density), Cyl—Cylindrical Lens, BS—Cube Beam Splitter. Obj—Objective Lenses, Ref—Reference Interface (Flat glass surface), Col—Collection Lens, BI CCD—Back Illuminated Charged Couple Device camera (iVac, Andor, UK); (**Right**) FF-OCT setup, LED—Light Emitting Diode, L1, L2, and L3—Achromatic lenses, RM—Reference Mirror, CMOS—Complementary Metal Oxide Semiconductor camera (Point Grey, GS3-U3-23S6M-C).

Table 1. Comparison of the specification of the LF and FF (full field) OCT devices, as used in the study.

Performance Parameter	LF-OCT	FF-OCT
Acquisition time (ms)	60	40,000
Acquired Image Pixels	1 × 256 × 1000	1920 × 1200 × 4000
Axial Resolution ($n_G \cdot \mu m$)	2.1	3.6
Lateral Resolution (μm)	18	4.4
Signal to Noise Ratio (dB)	79	54
Sensitivity (dB)	93	54

2.2. Samples

Four metallic car paint demo panels, one Indus silver, one Mauritius blue, one Barolo black, and one Santorini black were used in this study. These panels were examples of a common automotive multilayer coating system. The top layer was a clear coat with thickness to be measured. The second layer contains metallic flakes at random depths. For the silver and blue panels, a 2.25 mm × 1.4 mm area was masked off, and for cross validation purpose both instruments measured a B-Scan across the middle. The difference in positions between the scans was less than 1 mm. For a broader range of samples, the two different black samples were measured with the LF-OCT system only.

2.3. Software and Algorithm

The thicknesses of the clear coat and basecoat layers were calculated by determining the interface contours of the visible layers from the resulting B-scan images using a hierarchical graph-search approach. This assumed that volume scattering rather than interface reflection dominated the imaged layer boundaries, which was correct for all interfaces other than the surface in our data. The surface position was found by taking the average of the top two found profiles. Variational modelling inspired post-processing then improved robustness of the graph search approach by building in region intensity information. We first constructed a graph of nodes and edges using the image such that each pixel corresponded to a node. We thus redefined the segmentation as a minimal

cost graph cut problem; that is, the total cost of moving from one side of the graph to the other across the nodes whose values were determined by an energy functional aiming to split the image based on the gradient. To reduce the likelihood of jumping between interfaces, we defined our energy functional as $\mathcal{E}_j(\boldsymbol{x}) = (-1)^j(d_1\partial z(\boldsymbol{x})/\partial x_1 + d_2\partial z(\boldsymbol{x})/\partial x_2)$ where $z(\boldsymbol{x})$ denoted the image to be segmented, $\boldsymbol{x} = (x_1, x_2)^\top$, x_1 and x_2 are the coordinates in the lateral and depth directions, respectively, $d_1, d_2 \in \mathbb{R}_{>0}$ are non-negative parameters controlling the influence of the lateral and depth gradients, and $j \in \{0, 1\}$ determines whether we are seeking an upper or lower boundary.

Dynamic programming was used to find the path of minimal energy cost leading from the left-hand side of the image to the right. Calculating the cost of every possible path across the image would have been time consuming and necessitated storing a large amount of information. To avoid this, the paths were calculated in a structured manner with constraints inbuilt. From each (starting) pixel in the far-left A-Scan, we considered the cost of traversing a sub-path to another pixel in the following column, restricting the set of possible destination pixels to include only those within two rows. For each column, we stored the minimum cost movement only, and this process was repeated until the right-hand side of the image was reached. As well as resulting in a significant reduction in the number of required computations, the restrictions on the potential paths allowed also acted as regularisation on the length of the contour. Once the cumulative costs of the paths from each starting pixel were calculated, the overall minimum cost path could be found. This was done for each interface in a hierarchical way, excluding the nodes assigned to a contour to rule out crossing, defining the segmentation contours $\mathcal{S}_1, \ldots, \mathcal{S}_5 \in \mathbb{R}^n_>$.

Following this, we aimed to remove one surplus contour, leaving us with the best-fit segmentation of the image. We adopted the logic used for contour-fitting in variational methods such as [32,47]. In particular, we referred to the multi-phase work of Vese and Chan [47], which defined contours as level-sets [48] of a single function $\phi(\boldsymbol{x})$, and considered the correct segmentation as that which minimised the fitting energy only, since we did not need regularisation of the contour length. We identified the contour $\mathcal{S}_\kappa$ to be removed by determining the index κ which solved the minimisation problem

$$\min_{\kappa} \left\{ \sum_{\substack{i=0 \\ i \neq \kappa+1}}^{5} \int_{\Omega} \left(z - c_i^\kappa\right)^2 \mathcal{H}_i(\phi, l)\mathrm{d}\boldsymbol{x} \right\}, \; c_i^\kappa = \frac{\int_\Omega z\mathcal{H}_i(\phi,l)\mathrm{d}\boldsymbol{x} + \delta_i(\kappa)\int_\Omega z\mathcal{H}_{i+1}(\phi,l)\mathrm{d}\boldsymbol{x}}{\int_\Omega \mathcal{H}_i(\phi,l)\mathrm{d}\boldsymbol{x} + \delta_i(\kappa)\int_\Omega \mathcal{H}_{i+1}(\phi,l)\mathrm{d}\boldsymbol{x}}, \tag{1}$$

where $\mathcal{H}_i(\phi, l) = H^{\chi_1}(\phi - l_i)H^{\chi_2}(l_{i+1} - \phi)$ where $\chi_1 = 0$ for $i = 0$ and $\chi_1 = 1$ otherwise, $\chi_2 = 0$ for $i = 5$ and $\chi_2 = 1$ otherwise. Excluding $\mathcal{S}\_\kappa$ and ordering the sets in decreasing total sum, we obtained the list of contours $\mathcal{T}_1, \ldots, \mathcal{T}_4$. We then took the average of the top two contours which gave the upper and lower boundaries of the clear coat-air interface as its location. We could then give the thickness measurements of the clear coat ($\mathcal{T}_c$) and base coat ($\mathcal{T}_b$) layers as the pointwise difference of the sets $\mathcal{T}_c = \wp \cdot \left(\frac{\mathcal{T}_1 + \mathcal{T}_2}{2} - \mathcal{T}_3\right)$, $\mathcal{T}_b = \wp \cdot (\mathcal{T}_3 - \mathcal{T}_4)$, where $\wp$ was the pixel-size in the depth direction. The overall algorithm is shown in Figure 2 below.

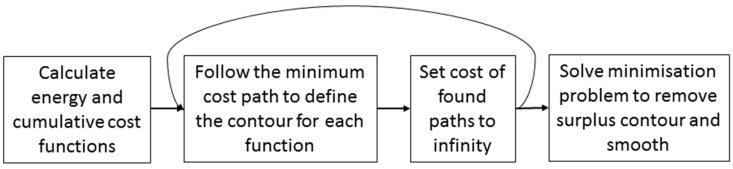

Figure 2. Flow chart of the segmentation process. The energy functional and cumulative cost functions are calculated to determine the minimal cost paths. Once all paths are found, the minimisation problem given in Equation (1) is solved to remove one contour, resulting in the set of segmentations.

3. Results

3.1. OCT Images

Figure 3 shows the OCT B-Scan images obtained for each panel. For Indus silver and Mauritius blue, the images from both LF-OCT and FF-OCT systems are compared. Both instruments give similar images, showing a larger optical thickness for the clear coating on the blue panel. Both instruments also show similar trends in the differences in appearance of the second layer of the two samples. Within the second layers, the signal contrast between the bright flakes and points in between is lower for the blue panel than the silver panel. To give the blue colour, the blue panel second layer may contain blue pigment particles, which would add to the scattering signal between flakes. The main difference between the images from the two instruments is the lateral resolution. The resolved flakes from the high lateral resolution FF-OCT appear narrower than for the LF-OCT, where the lower lateral resolution has broadened their apparent width. Both (i.e., Barolo and Santorini) black LF-OCT images are significantly different, compared with silver and blue, with the visible base coat thickness being much thinner. The clear coat of Santorini black is the thinnest of all the samples.

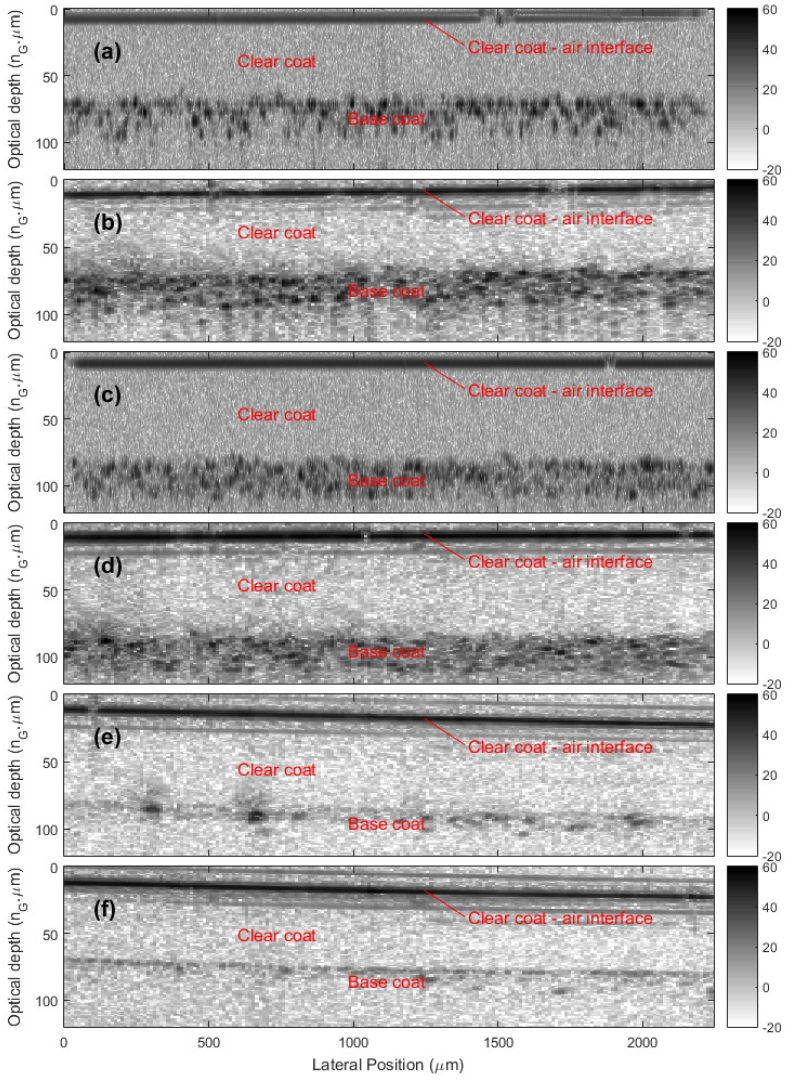

Figure 3. B-Scan images of Indus silver (**a**,**b**), Mauritius blue (**c**,**d**), Barolo black (**e**), and Santorini black (**f**) automotive metallic paint samplers. Taken with FF-TD (**a**,**c**) and LF-FD (**b**,**d**–**f**) parallel OCT systems. The FF-OCT B-Scans are taken from within 1 mm of the location of the corresponding LF-OCT images. Scaling is the same for all images. Colour bar units are dB.

Though the relatively lower lateral resolution of the LF-OCT has partially blurred the second layer, it is still sufficient to resolve the image texture. Figure 4 (top) shows the LF-OCT B-Scan of the silver panel (same as Figure 3b) with two A-Scan locations (red and blue) marked on. Figure 4 (bottom) is the plot of the intensity of these two A-Scans, and the apparent thickness estimated from obvious peaks. Considering these (red and blue) A-Scans separately and without prior knowledge of the sample, as would be the case in a single point measurement, their interpretations give a large difference in the thickness measurement of the clear coat. In this case, for the red A-Scan the apparent signal for the second interface comes from far too deep. No reasonable estimate of the base coat layer could be made without prior knowledge of the A-Scan properties for the sample. In contrast to this lack of information in the 1D single point measurement, in the 2D B-Scan image the layers and their boundaries are immediately visibly apparent without any prior knowledge. In this case the source of the error for the clear coat thickness in the single point measurement is the dominating signal from the metal flakes, which at any given lateral position could be present at any depth within the second layer. For a single point system, to reliably overcome this, the user could take multiple measurements at different sample positions and use the averaged A-scan signal for thickness calculation. However, we will show that reliable coating thickness and uniformity information could be obtained by using the single shot LF-OCT system and automated image segmentation algorithms, without the need for multiple measurements.

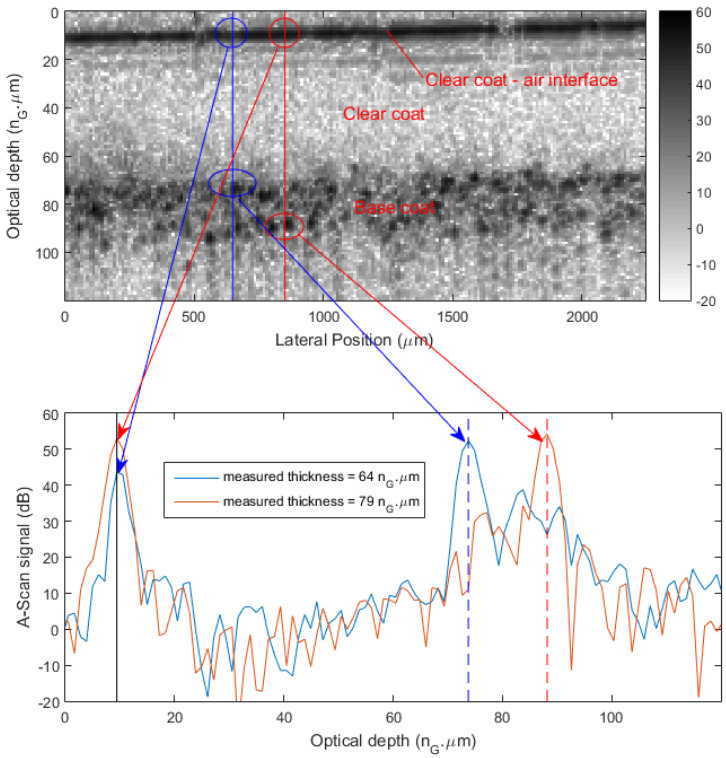

Figure 4. (**Top**) LF-FD-OCT image of silver metallic paint sampler (Figure 3b) with two (blue and red) A-Scan locations marked. (**Bottom**) Plot of the red and blue A-Scans, with the apparent thickness measured using only the single A-Scan data. The arrows show the correspondence of the A-Scan peaks with location in the B-Scan image.

3.2. Automated Segmentation of Layer Thickness

We now calculate the thickness of the clear coat and base coat layers of the paint samples across the whole B-scan image. We first partition the image to identify the layers automatically using the graph search approach described in the previous section. Using forward first order finite differences as a discrete approximation to the derivative, we calculate the energy functional as an important step in

identifying the contours. An example of this using the silver sample is shown for $j = 0$ and $j = 1$ in Figure 5a,b respectively. The lower values corresponding to the minimiser appear as the darker colour in the figure and are to be traced automatically. While the lowest intensity path may appear clear in each figure, the remaining paths are difficult to trace by sight. Proceeding hierarchically with the graph search approach, we obtain a set of potential interface contours (Figure 5c) which closely match the visible edges. An additional phantom contour is also found which does not represent a layer boundary but does correspond to a solution of the graph-search problem. We now employ our data-fitting step to remove this contour (Figure 5d). At this point, we have a close segmentation of each layer given the presentation of the paint samples in the image.

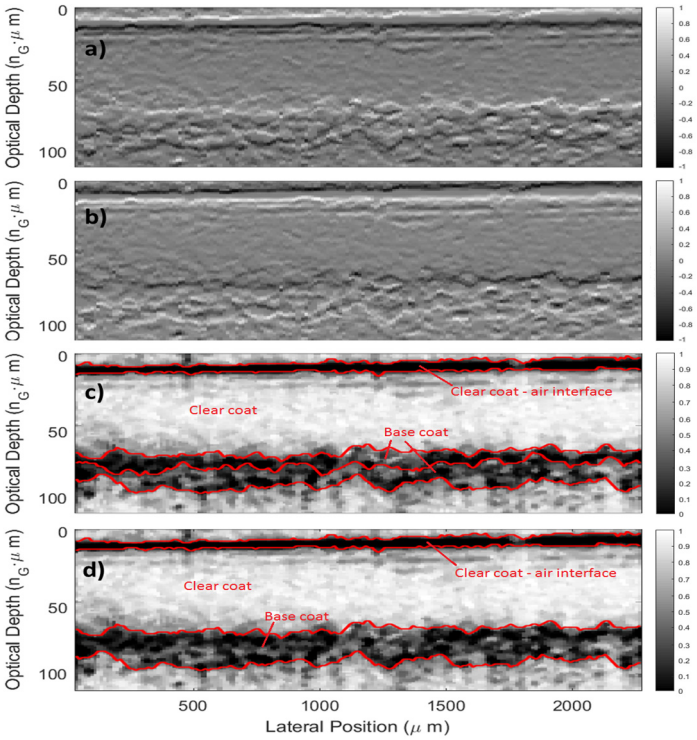

Figure 5. Segmentation process of LF-OCT B-scan of silver car paint sample. (**a**,**b**) The joint energy functional used to find the initial contours; (**c**) The initial result using graph-search segmentation; (**d**) The result after automated removal of the phantom contour.

As a final step, we compensate for the visible blurring of the air-clear coat layer interface by replacing the two boundary contours with their mean value to obtain the final segmentation of the silver sample shown in Figure 6a. The same procedure is applied to the blue paint sample and the contours are correctly identified in Figure 6c. It is now a simple procedure to obtain the thickness measurements of each layer across the whole B-Scan (Figure 6b,d). Table 2 gives the mean and standard deviation of these measured thicknesses of the clear coating and base coat, within a B-Scan measurement, for the two samples with both OCT instruments. However, it should be noted that this standard deviation does not have a clear relationship with accuracy or precision of the mean value. The variance is caused by the apparent interface texture in the image, which may be real or, as quite likely in this case, a result of the volume scattering properties of one of the layers. Here reflections from the semi-sparse metallic flakes within the base coat layer dominate giving a lumpy image signal, which the graph search algorithm traces over. The repeatability (precision), for the LF-OCT, of the mean clear and base coat thickness values was quantified by measuring at eight locations on the Indus silver sample, the standard deviation was 2 and 5 $n_G \cdot \mu$m, respectively. The accuracy is determined by the axial resolution (systematic biasing of graph search algorithm to one side of the interface will be of this order

of magnitude) and/or scattering homogeneity of the layers (non-homogeneous properties causing the apparent profile undulate into the layer, as is likely in these results). If we treat these as standard error, the accuracy for the given Indus Silver sample LF-OCT measurement is then calculated to be 3 and 4 $n_G \cdot \mu m$ for the clear and base coat, respectively. In Table 2, the largest difference in mean thickness of both techniques is 3 $n_G \cdot \mu m$ for the base coat, which is within the measured undulation, precision, and calculated accuracy values of the LF-OCT. The differences in the mean values for the clear coat are negligible. Therefore, we conclude that the segmentation algorithm gives repeatable (within the technique's measured errors) measurements independent of the OCT instrument. It should be noted that for optical techniques, the precision and accuracy of the measurement of an interface is highly dependent on the sample. For an interface that gives a significant signal, profilometry techniques are able to measure it with high accuracy. However, in this case the signal from the interface is negligible, with the image contrast being dominated by volume scattering; as such, profilometry methods would not work, and image segmentation is the preferred technique. The alternative would be to correct the B-Scan image by rotation for any tilt, and then average the A-Scans. However, this would eliminate lateral spatial information that may be present.

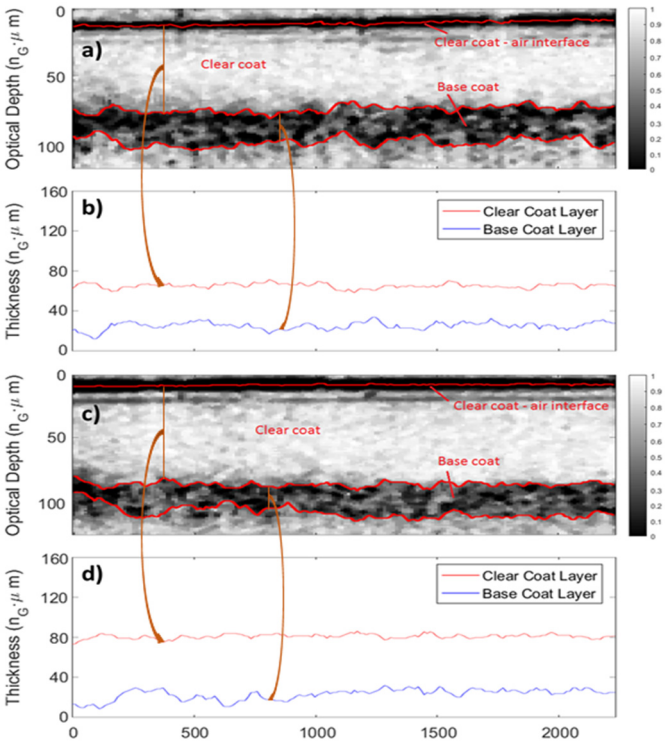

Figure 6. Final segmentation results of the silver (**a**) and blue (**c**) paint samples. The respective thickness profiles of each sample (**b**,**d**) as demonstrated by the brown arrows. Although they do look non-smooth, it should be noted that the thickness profile figures are presented at an aspect ratio of approximately 1:3.

Table 2. Thickness measurements (mean ± standard deviation) of the base coat and clear coat layers of the paint samples scanned using full field time domain (FF) and line field spectral domain (LF) OCT.

Sample	Method	Base Coat Layer Thickness ($n_G \cdot \mu m$)	Clear Coat Layer Thickness ($n_G \cdot \mu m$)
Indus Silver	FF-OCT	27.88 ± 6.11	65.64 ± 1.34
Indus Silver	LF-OCT	24.95 ± 3.85	64.98 ± 2.44
Mauritius Blue	FF-OCT	25.83 ± 4.62	80.75 ± 1.44
Mauritius Blue	LF-OCT	22.69 ± 5.47	80.68 ± 2.20
Barlo Black	LF-OCT	16.61 ± 4.48	68.96 ± 2.01
Santorini Black	LF-OCT	8.13 ± 3.24	54.50 ± 2.30

4. Discussion

Industrial coatings are economically important. Their QA measurement is important to ensure protection and appearance consistency. To measure the thickness of coating layers, contact single point techniques currently dominate the market. These can only give limited spatial information and may require multiple measurements to ensure accuracy. As shown here, LF-OCT returns to the user a 2D cross-sectional image of non-opaque coatings where both coating thickness and coating uniformity information can be extracted. To collect 2D images, conventional point by point raster scanning OCT requires mechanical scanning of the probe beam across the sample. This adds complexity, and potential fragility, for a challenging industrial environment. In contrast, the proposed LF-OCT imaging requires no mechanical scanning, thus it is an attractive solution for the application. It requires no mechanical moving parts, thus it should increase the robustness of the technique in dirty and rough industrial environments.

Segmentation can be used to extract dimensions automatically from images. To measure the thickness of coating layers from OCT B-Scan images, graph search has been shown to be a robust and fast method. The image segmentation technique can be applied to any B-Scan image of layered structures, independent of the OCT instrument. Here, we showed this robustness by applying an algorithm to data taken using two OCT systems with different imaging specifications and modalities, and recorded matching results within the standard deviation of the thickness profiles. It should also be noted that a 2D B-Scan image, not a full 3D measurement, is required for this reliable thickness measure, which is provided by LF-OCT without any electro-mechanical scanning. Also, the presence and magnitude of any significant non-uniformity of coating thickness, over the lateral dimension of measurement, would be as apparent in this 1D measurement from the 2D B-Scan, as it would in a 2D map from a 3D volume scan. A 2D map of coating thickness in the local area of measurement would not provide any significant further information for the QA measure, which ultimately is required to give a binary pass or fail output.

Currently as presented, the instrument is still of significant cost and size. To be viable against competing techniques, future work must reduce the cost and size of such a device. However, there is potential for reducing the cost of a device by reducing the specification for all the components. Thermal light sources have previously [28] been demonstrated to be suitable for LF-OCT, and during the development of our LF-OCT instrument we successfully used an incandescent bulb of negligible cost to take images. The drawback of thermal sources is that adaption to compensate for low spatial coherence will lead to a slower measurement time. However, this will still be under 1 s so would not be an issue for this application. Also, thermal sources will not be a factor in restricting the bandwidth used, so will allow high axial resolutions to be achieved. The imaging spectrograph part of the device can be constructed, to a reduced size, with off the shelf components of minimum cost. With operation between optical and Near InfraRed (NIR) wavelengths of 400 to 1000 nm, a low cost CMOS camera array can be used. The drawback of this is likely to be on the spectral resolution, which will limit image depth. However, reduction of size favours spectral bandwidth and thus high image axial resolution. The use of a LF-OCT, rather than the more common point by point raster scanning OCT, arrangement would mean no mechanical moving parts would be required. Future work will involve construction and testing of this proposed low cost device. As well as application to automotive coatings, the combination of the low cost LF-OCT device and graph search segmentation could be used for industrial coatings on wood [2] and in aerospace applications, such as thermal barrier coatings for aerospace turbine blades [49]. It may also be used for the automatic measurement of pharmaceutical tablet coating thicknesses [50].

In conclusion, we have demonstrated the use of LF-OCT to take cross sectional (B-Scan) images of optically transparent coatings without moving parts. Combining this with fast automated graph search image sectioning allows reliable thickness profiles to be calculated with a single, scan-less, LF-OCT measurement. We have illustrated that a single point measurement of layer thickness is inherently less reliable than a measurement from a B-Scan image. The combining of these methods

gives a clear development path for a new reliable and cost competitive instrument for the QA of certain industrial coatings.

Acknowledgments: The Ultrasensitive Optical Coherence Tomography Imaging for Eye Disease is funded by the National Institute for Health Research's i4i Programme. This paper summarises independent research funded by the National Institute for Health Research (NIHR) under its i4i Programme (Grant Reference Number II-LA-0813-20005). The views expressed are those of the authors and not necessarily those of the NHS, the NIHR, or the Department of Health. This work is partly supported by the UK EPSRC Research Grant No. EP/L019787/1. The authors thank Roy Donga of Jaguar Land Rover Limited for providing the test samples.

Author Contributions: Samuel Lawman wrote the majority of the paper and conducted the LF-OCT measurements; Bryan M. Williams wrote the minority of the paper and conducted the image segmentation; Jinke Zhang conducted the FF-OCT measurements; Yao-Chun Shen provided the original paper idea and oversaw the LF-OCT and FF-OCT hardware; Yalin Zheng was the LF-OCT project instigator and oversaw the image segmentation work.

Conflicts of Interest: The authors declare no conflict of interest. The founding sponsors had no role in the design of the study; in the collection, analyses, or interpretation of data; in the writing of the manuscript, and in the decision to publish the results.

References

1. Akafuah, N.K.; Poozesh, S.; Salaimeh, A.; Patrick, G.; Lawler, K.; Saito, K. Evolution of the automotive body coating process—A review. *Coatings* **2016**, *6*, 24. [CrossRef]
2. Evans, P.D.; Haase, J.G.; Shakri, B.; Kiguchi, M. The search for durable exterior clear coatings for wood. *Coatings* **2015**, *5*, 830–864. [CrossRef]
3. Lawman, S.J. *Optical and Material Properties of Varnishes for Paintings*; Nottingham Trent University: Nottingham, UK, 2011.
4. Matheson, R.R. Paint and coatings technology: Current industrial trends. *Polym. Rev.* **2006**, *46*, 341–346. [CrossRef]
5. Hayes, G.E. *Quality Assurance: Management & Technology*, 2nd ed.; Charger Productions: Capistrano Beach, CA, USA, 1976.
6. Brasunas, J.C.; Cusham, G.M.; Lakew, B. Thickness measurement. In *The measurement, Instrumentation and Sensors: Handbook*; Webster, J.G., Ed.; CRC Press: Boca Raton, FL, USA, 1999.
7. Szabo, T.L. *Diagnostic Ultrasound Imaging: Inside Out*, 2nd ed.; Academic Press: Oxford, UK, 2014.
8. Tam, A.C. Pulsed-laser generation of ultrashort acoustic pulses—Application for thin-film ultrasonic measurements. *Appl. Phys. Lett.* **1984**, *45*, 510–512. [CrossRef]
9. White, J.S.; LaPlant, F.P.; Dixon, J.W.; Emch, D.J.; Datillo, V.P. Non-Contact Real-Time Film Thickness Gage for Automotive Body Painting Applications. *SAE Tech. Paper* **1998**. [CrossRef]
10. Su, K.; Shen, Y.C.; Zeitler, J.A. Terahertz sensor for non-contact thickness and quality measurement of automobile paints of varying complexity. *IEEE Trans. Terahertz Sci. Technol.* **2014**, *4*, 432–439. [CrossRef]
11. Ling, X.; Pritzker, M.D.; Byerley, J.; Burns, C.M. Confocal scanning laser microscopy of polymer coatings. *J. Appl. Polym. Sci.* **1998**, *67*, 149–158. [CrossRef]
12. Miller, D.A. *Optical Properties of Solid Thin Films by Spectroscopic Reflectometry and Spectroscopic Ellipsometry*; City University of New York: New York, NY, USA, 2008.
13. Garcia-Caurel, E.; De Martino, A.; Gaston, J.P.; Yan, L. Application of spectroscopic ellipsometry and mueller ellipsometry to optical characterization. *Appl. Spectrosc.* **2013**, *67*, 1–21. [CrossRef] [PubMed]
14. Stifter, D. Beyond biomedicine: A review of alternative applications and developments for optical coherence tomography. *Appl. Phys. B* **2007**, *88*, 337–357. [CrossRef]
15. Liang, H.; Cid, M.G.; Cucu, R.G.; Dobre, G.M.; Podoleanu, A.G.; Pedro, J.; Saunders, D. En-face optical coherence tomography—A novel application of non-invasive imaging to art conservation. *Opt. Express* **2005**, *13*, 6133–6144. [CrossRef] [PubMed]
16. Latour, G.; Echard, J.P.; Soulier, B.; Emond, I.; Vaiedelich, S.; Elias, M. Structural and optical properties of wood and wood finishes studied using optical coherence tomography: Application to an 18th century italian violin. *Appl. Opt.* **2009**, *48*, 6485–6491. [CrossRef] [PubMed]

17. Meemon, P.; Yao, J.N.; Lee, K.S.; Thompson, K.P.; Ponting, M.; Baer, E.; Rolland, J.P. Optical coherence tomography enabling non destructive metrology of layered polymeric grin material. *Sci. Rep.* **2013**, *3*, 1709. [CrossRef]
18. Dong, Y.; Lawman, S.; Zheng, Y.L.; Williams, D.; Zhang, J.K.; Shen, Y.C. Nondestructive analysis of automotive paints with spectral domain optical coherence tomography. *Appl. Opt.* **2016**, *55*, 3695–3700. [CrossRef] [PubMed]
19. Zhang, N.; Wang, C.M.; Sun, Z.W.; Mei, H.C.; Huang, W.; Xu, L.; Xie, L.C.; Guo, J.J.; Yan, Y.W.; Li, Z.H.; et al. Characterization of automotive paint by optical coherence tomography. *Forensic Sci. Int.* **2016**, *266*, 239–244. [CrossRef] [PubMed]
20. Lawman, S.; Liang, H.D. High precision dynamic multi-interface profilometry with optical coherence tomography. *Appl. Opt.* **2011**, *50*, 6039–6048. [CrossRef] [PubMed]
21. Duma, V.F.; Tankam, P.; Huang, J.X.; Won, J.; Rolland, J.P. Optimization of galvanometer scanning for optical coherence tomography. *Appl. Opt.* **2015**, *54*, 5495–5507. [CrossRef] [PubMed]
22. Watanabe, Y.; Yamada, K.; Sato, M. Three-dimensional imaging by ultrahigh-speed axial-lateral parallel time domain optical coherence tomography. *Opt. Express* **2006**, *14*, 5201–5209. [CrossRef] [PubMed]
23. Povazay, B.; Unterhuber, A.; Hermann, B.; Sattmann, H.; Arthaber, H.; Drexler, W. Full-field time-encoded frequency-domain optical coherence tomography. *Opt. Express* **2006**, *14*, 7661–7669. [CrossRef] [PubMed]
24. Fechtig, D.J.; Schmoll, T.; Grajciar, B.; Drexler, W.; Leitgeb, R.A. Line-field parallel swept source interferometric imaging at up to 1 MHz. *Opt. Lett.* **2014**, *39*, 5333–5336. [CrossRef] [PubMed]
25. Zuluaga, A.F.; Richards-Kortum, R. Spatially resolved spectral interferometry for determination of subsurface structure. *Opt. Lett.* **1999**, *24*, 519–521. [CrossRef] [PubMed]
26. Grajciar, B.; Pircher, M.; Fercher, A.F.; Leitgeb, R.A. Parallel fourier domain optical coherence tomography for in vivo measurement of the human eye. *Opt. Express* **2005**, *13*, 1131–1137. [CrossRef] [PubMed]
27. Zhang, Y.; Rha, J.T.; Jonnal, R.S.; Miller, D.T. Adaptive optics parallel spectral domain optical coherence tomography for imaging the living retina. *Opt. Express* **2005**, *13*, 4792–4811. [CrossRef] [PubMed]
28. Graf, R.N.; Brown, W.J.; Wax, A. Parallel frequency-domain optical coherence tomography scatter-mode imaging of the hamster cheek pouch using a thermal light source. *Opt. Lett.* **2008**, *33*, 1285–1287. [CrossRef] [PubMed]
29. Robles, F.E.; Wilson, C.; Grant, G.; Wax, A. Molecular imaging true-colour spectroscopic optical coherence tomography. *Nat. Photon.* **2011**, *5*, 744–747. [CrossRef] [PubMed]
30. Chen, Z.Y.; Zhao, C.; Shen, Y.; Li, P.; Wang, X.P.; Ding, Z.H. Ultrawide-field parallel spectral domain optical coherence tomography for nondestructive inspection of glass. *Opt. Commun.* **2015**, *341*, 122–130. [CrossRef]
31. Mumford, D.; Shah, J. Optimal approximation by piecewise smooth functions and associated variational problems. *Commun. Pur. Appl. Math.* **1989**, *42*, 577–685. [CrossRef]
32. Chan, T.F.; Vese, L.A. Active contours without edges. *IEEE Trans. Image Process.* **2001**, *10*, 266–277. [CrossRef] [PubMed]
33. Vermeer, K.; Van der Schoot, J.; Lemij, H.; De Boer, J. Automated segmentation by pixel classification of retinal layers in ophthalmic oct images. *Biomed. Opt. Express* **2011**, *2*, 1743–1756. [CrossRef] [PubMed]
34. Garvin, M.K.; Abràmoff, M.D.; Kardon, R.; Russell, S.R.; Wu, X.; Sonka, M. Intraretinal layer segmentation of macular optical coherence tomography images using optimal 3-D graph search. *IEEE T. Med. Imaging* **2008**, *27*, 1495–1505. [CrossRef] [PubMed]
35. Shen, M.; Cui, L.; Li, M.; Zhu, D.; Wang, M.R.; Wang, J. Extended scan depth optical coherence tomography for evaluating ocular surface shape. *J. Biomed. Opt.* **2011**, *16*, 056007. [CrossRef] [PubMed]
36. Otsu, N. A threshold selection method from gray-level histograms. *Automatica* **1975**, *11*, 23–27. [CrossRef]
37. Ambrosio, L.; Tortorelli, V.M. On the approximation of free discontinuity problems. *Bollettino dell'Unione Mathematica Italiana B* **1992**, *7*, 105–123.
38. Rada, L.; Chen, K. A new variational model with dual level set functions for selective segmentation. *Commun. Comput. Phys.* **2012**, *12*, 261–283. [CrossRef]
39. Williams, B.M.; Spencer, J.A.; Chen, K.; Zheng, Y.; Harding, S.P. An effective variational model for simultaneous reconstruction and segmentation of blurred images. *J. Algorithms Comput. Technol.* **2016**, *10*, 244–264. [CrossRef]
40. Fuller, A.; Zawadzki, R.; Choi, S.; Wiley, D.; Werner, J.; Hamann, B. Segmentation of three-dimensional retinal image data. *IEEE Trans. Vis. Comput. Graph.* **2007**, *13*, 1719–1726. [CrossRef] [PubMed]

41. Bae, E.; Tai, X.-C. Graph cut optimization for the piecewise constant level set method applied to multiphase image segmentation. In *Scale Space and Variational Methods in Computer Vision*; Springer: Berlin, Germany, 2009; pp. 1–13.
42. LaRocca, F.; Chiu, S.J.; McNabb, R.P.; Kuo, A.N.; Izatt, J.A.; Farsiu, S. Robust automatic segmentation of corneal layer boundaries in sdoct images using graph theory and dynamic programming. *Biomed. Opt. Express* **2011**, *2*, 1524–1538. [CrossRef] [PubMed]
43. Williams, D.; Zheng, Y.; Bao, F.; Elsheikh, A. Fast segmentation of anterior segment optical coherence tomography images using graph cut. *Eye Vis.* **2015**, *2*, 1. [CrossRef] [PubMed]
44. Boykov, Y.; Kolmogorov, V. An experimental comparison of min-cut/max-flow algorithms for energy minimization in vision. *IEEE Trans. Pattern Anal. Mach. Intell.* **2004**, *26*, 1124–1137. [CrossRef] [PubMed]
45. Li, C.; Zeitler, J.A.; Dong, Y.; Shen, Y.-C. Non-destructive evaluation of polymer coating structures on pharmaceutical pellets using full-field optical coherence tomography. *J. Pharm. Sci.* **2014**, *103*, 161–166. [CrossRef] [PubMed]
46. Lawman, S.; Dong, Y.; Williams, B.M.; Romano, V.; Kaye, S.; Harding, S.P.; Willoughby, C.; Shen, Y.C.; Zheng, Y.L. High resolution corneal and single pulse imaging with line field spectral domain optical coherence tomography. *Opt. Express* **2016**, *24*, 2395–2405. [CrossRef] [PubMed]
47. Vese, L.A.; Chan, T.F. A multiphase level set framework for image segmentation using the mumford and shah model. *Int. J. Comput. Vis.* **2002**, *50*, 271–293. [CrossRef]
48. Osher, S.; Sethian, J.A. Fronts propagating with curvature-dependent speed: Algorithms based on Hamilton–Jacobi formulations. *J. Comput. Phys.* **1988**, *79*, 12–49.
49. Ellingson, W.A.; Visher, R.J.; Lipanovich, R.S.; Deemer, C.M. Optical nde methods for ceramic thermal barrier coatings. *Mater. Eval.* **2006**, *64*, 45–51.
50. Markl, D.; Zettl, M.; Hannesschlaeger, G.; Sacher, S.; Leitner, M.; Buchsbaum, A.; Khinast, J.G. Calibration-free in-line monitoring of pellet coating processes via optical coherence tomography. *Chem. Eng. Sci.* **2015**, *125*, 200–208. [CrossRef]

© 2017 by the authors. Licensee MDPI, Basel, Switzerland. This article is an open access article distributed under the terms and conditions of the Creative Commons Attribution (CC BY) license (http://creativecommons.org/licenses/by/4.0/).